

'Mito-Bomb': a novel mitochondria-targeting nanosystem for ferroptosis-boosted sonodynamic antitumor therapy

Jianxin Wang^a, Zhiyu Zhao^a, Yan Liu^a, Xinyu Cao^a, Fuxin Li^a, Haitao Ran^b, Yang Cao^b and Changjun Wu^a

^aDepartment of Ultrasound, The First Affiliated Hospital of Harbin Medical University, Harbin, China; ^bChongqing Key Laboratory of Ultrasound Molecular Imaging, Institute of Ultrasound Imaging, Second Affiliated Hospital, Chongqing Medical University, Chongqing, China

ABSTRACT

Mitochondria play an important role in regulating tumor cell death and metabolism so that they can be potential therapeutic targets. Sonodynamic therapy (SDT) represents an attractive antitumor method that induces apoptosis by producing highly toxic reactive oxygen species (ROS). Mitochondria-targeting SDT can cause oxidative damage and improve the efficiency of tumor therapy. However, due to the nonselective distribution of nanosystems and the anti-apoptotic mechanism of cancer cells, the therapeutic effect of SDT is not ideal. Therefore, we proposed a novel mitochondria-targeting nanosystem ('Mito-Bomb') for ferroptosis-boosted SDT. Sonosensitizer IR780 and ferroptosis activator RSL-3 were both encapsulated in biocompatible poly(lactic-co-glycolic acid) (PLGA) nanoparticles to form 'Mito-Bomb' (named IRP NPs). IR780 in this nanosystem was used to mediate mitochondria-targeting SDT. RSL-3 inhibited the activity of GPX4 in the antioxidant system to induce ferroptosis of tumor cells, which could rewire tumor metabolism and make tumor cells extremely sensitive to SDT-induced apoptosis. Notably, we also found that RSL-3 can inhibit hypoxia inducible factor-1 α (HIF-1 α) and induce ROS production to improve the efficacy of SDT to synergistically antitumor. RSL-3 was applied as a 'One-Stone-Three-Birds' agent for cooperatively enhanced SDT against triple-negative breast cancer. This study presented the first example of RSL-3 boosting mitochondria-targeting SDT as a ferroptosis activator. The 'Mito-Bomb' biocompatible nanosystem was expected to become an innovative tumor treatment method and clinical transformation.

Abbreviations: SDT, sonodynamic therapy; ROS, reactive oxygen species; PLGA, poly(lactic-co-glycolic acid); HIF-1 α , hypoxia inducible factor-1 α ; TNBC, triple-negative breast cancer tumor; LPO, lipid peroxidation; GPX4, GSH glutathione peroxidase 4; PAI, photoacoustic imaging; DII, 1,1-dioctadecyl-3,3,3',3'-tetramethylindocarbocyanine perchlorate; PVA, polyvinyl alcohol; DCFH-DA, 2'-7'-dichlorofluorescein diacetate; JC-1, 5,5',6,6'-tetrachloro-1,1',3,3'-tetraethyl-imidacarbocyanine iodide; DAPI: 4,6-diamidino-2-phenylindole; CCK-8, Cell Counting Kit-8; CH₂Cl₂: dichloromethane; DLS, dynamic light scattering; PBS, phosphate buffered saline; HPLC, high-performance liquid chromatography; CLSM, confocal laser scanning microscope; US, ultrasound; IP NPs: IP780-PLGA NPs; IRP NPs, IP780-RSL-3-PLGA NPs; WB, western blot; TUNEL, TdT-mediated dUTP nick-end labeling; H&E, hematoxylin-eosin staining

ARTICLE HISTORY

Received 26 July 2022
Revised 6 September 2022
Accepted 12 September 2022



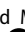
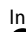
KEYWORDS


Sonodynamic therapy; ferroptosis; reactive oxygen species; GPX4; RSL-3

1. Introduction

Sonodynamic therapy (SDT), as a new treatment strategy for tumor treatment, has overcome the limitation of light penetration depth and has the advantages of minimally invasive, no radiation, and low cost (Lafond et al., 2019; Son et al., 2020; Jiang et al., 2022). Although the detailed mechanism of SDT is still unclear, it is evident that low-intensity ultrasound will lead to excessive reactive oxygen species (ROS) production when interacting with sonosensitizers, thus enhancing cytotoxicity (Son et al., 2020; Zhang et al., 2021b). In addition, an essential factor affecting SDT is the subcellular localization of sonosensitizers. Mitochondria, as the site of cell energy metabolism,

also participate in various types of cell death, which has attracted the attention of researchers (Pathania et al., 2009; Guo et al., 2021). Previous studies have shown that destroying mitochondrial integrity can transmit apoptotic cell signals and initiate apoptosis. Mitochondria-targeting SDT resulted in more tumor cell apoptosis than SDT with nonselective subcellular distribution (Zong et al., 2016; Qu et al., 2020; Han et al., 2021). Therefore, mitochondria-targeting SDT is considered a more effective and promising treatment for apoptosis. However, due to the inherent anti-apoptotic ability of triple-negative breast cancer tumor (TNBC) cells, the overall effectiveness of various treatment methods, including SDT and the improvement of patient survival rate, are still not ideal (Sun et al., 2021; Yao

CONTACT Yang Cao  yangcao@cqmu.edu.cn  Chongqing Key Laboratory of Ultrasound Molecular Imaging, Institute of Ultrasound Imaging, Second Affiliated Hospital, Chongqing Medical University, Chongqing 400010, China or Changjun Wu  bccjw@sohu.com  Department of Ultrasound, The First Affiliated Hospital of Harbin Medical University, Harbin 150001, China.

 Supplemental data for this article can be accessed online at <https://doi.org/10.1080/10717544.2022.2126027>.

© 2022 The Author(s). Published by Informa UK Limited, trading as Taylor & Francis Group.

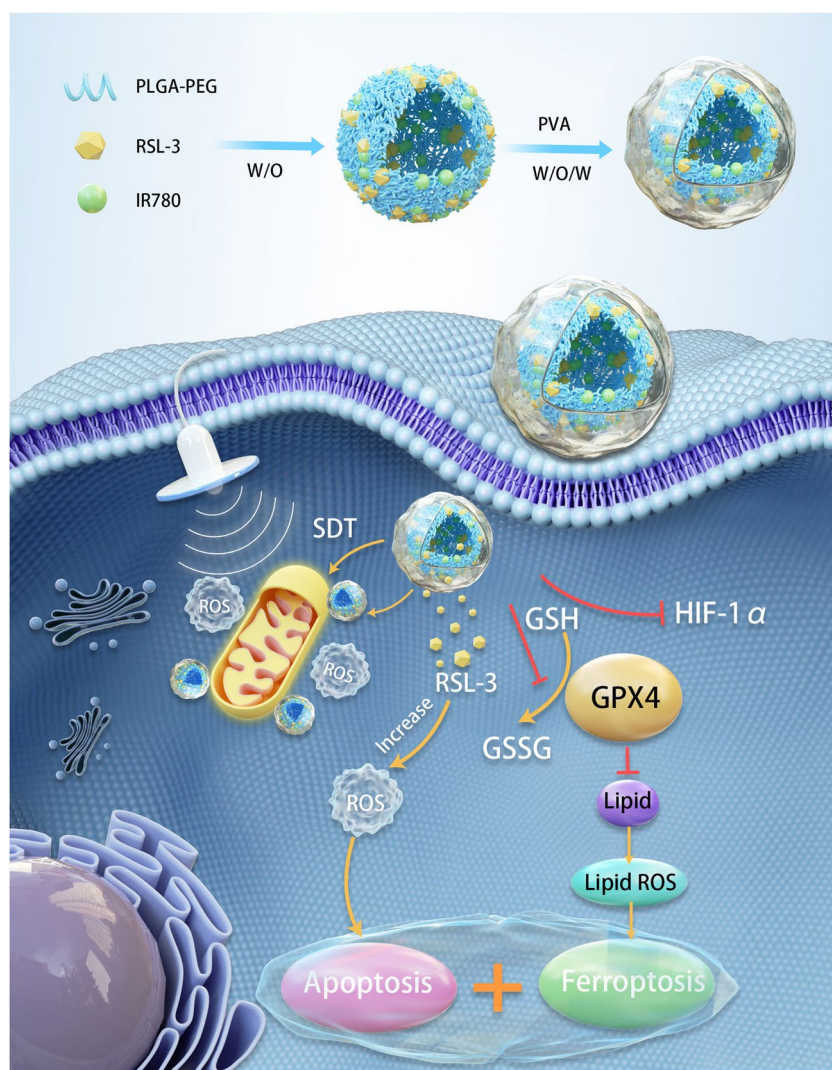
This is an Open Access article distributed under the terms of the Creative Commons Attribution License (<http://creativecommons.org/licenses/by/4.0/>), which permits unrestricted use, distribution, and reproduction in any medium, provided the original work is properly cited.

et al., 2021). There is an urgent need to develop non-apoptotic therapies to disrupt the anti-apoptotic mechanisms of TNBC cells.

Ferroptosis differs from apoptosis and other types of cell death regulation in morphology and mechanism. Morphologically, it is characterized by the atrophy of mitochondria and a decrease in the number of mitochondrial cristae (Luo et al., 2021). As a cell death mode different from traditional apoptosis, ferroptosis can cause cell death by inhibiting the glutathione-dependent antioxidant defense mechanism and the uncontrolled production of lipid ROS catalyzed by iron ions, mainly the accumulation of lipid peroxidation (LPO) (Stockwell et al., 2017; Hirschhorn & Stockwell, 2019). This can overcome the limitations of existing antitumor therapies and enhance tumor treatment through synergistic effects with SDT. Glutathione peroxidase 4 (GPX4), mainly located in the cytoplasm, can be a core regulator of ferroptosis (Dixon et al., 2012; J. Li et al., 2020). GPX4 combats with LPO by using two glutathione molecules as electron donors to reduce cytotoxic LPO to the corresponding alcohols (Yang et al., 2014; Xu et al., 2021). Inhibiting GPX4 activity can lead to LPO accumulation, a significant feature of ferroptosis (Wei et al., 2020; Tang et al., 2021). In addition, studies

have also confirmed that direct targeting of GPX4 is more effective than the destruction of GSH in cancer treatment based on ferroptosis (Shintoku et al., 2017; X. Li et al., 2022). Methyl (1*S*,3*R*)-2-(2-chloroacetyl)-1-(4-(methoxycarbonyl)phenyl)-2,3,4,9-tetrahydro-1*H*-pyrido[3,4-*b*]indole-3-carboxylate (RSL-3) contains electrophilic chloroacetamide moiety, which irreversibly binds to its active site, directly inhibiting the catalytic activity of GPX4 (Eaton et al., 2020). Thus, the redox balance in tumor cells is destroyed, and ferroptosis is induced.

Capitalizing on these facts, we innovatively propose a novel mitochondria-targeting nanosystem ('Mito-Bomb') for ferroptosis-boosted SDT. We used FDA-approved degradable poly(lactic-co-glycolic acid) (PLGA) to encapsulate oil-soluble drugs IR780 and RSL-3 (Scheme 1). The problem of low solubility and poor pharmacokinetics of two drugs was solved by using PLGA as the carrier to improve the possibility of its clinical application. IR780 has been confirmed to accumulate in mitochondria preferentially (Wang et al., 2013; Zhang et al., 2018). IR780 mediates mitochondrial-targeted SDT and can perform visual and accurate treatment under photoacoustic imaging (PAI) guidance. PAI is a new noninvasive and non-ionizing biomedical imaging method developed in recent



Scheme 1.

years, which can monitor the treatment process in real time and visualize tumor treatment (Steinberg et al., 2019; Glickman, 2021). RSL-3 as a 'One-Stone-Three-Birds' agent for cooperatively enhanced SDT against breast cancer. RSL-3 has confirmed its sensitization effect on SDT in vitro and in vivo by simultaneously inhibiting GPX4 and hypoxia inducible factor-1 α (HIF-1 α) and promoting ROS production. The mitochondria-targeting nanosystem ('Mito-Bomb') can simultaneously ferroptosis-boosted SDT against TNBC. This nanosystem can accumulate into the tumor through intravenous injection and significantly inhibit tumor growth without any adverse side effects, which provides an avenue for therapeutic intervention against TNBC in the clinic.

2. Material and methods

2.1. Materials and reagents

PEGylated PLGA (50:50, PLGA 12,000Da MW, PEG 2,000Da MW) (PLGA-PEG_{2,000}) was purchased from Xi'an Ruixi Biological Technology Co., Ltd. (Shaanxi, China). IR780 iodide, 1,1-dioctadecyl-3,3,3',3'-tetramethylindocarbocyanine perchlorate (DiI), 2'-7'-dichlorofluorescein diacetate (DCFH-DA), and polyvinyl alcohol (PVA) were purchased from Sigma-Aldrich (St Louis, USA). RSL-3 was purchased from MedChemExpress (Shanghai, P.R. China). Anti-Caspase-3, anti-HIF-1 α , and anti-GPX4 antibodies were purchased from Abcam (London, U.K.). 5,5',6,6'-Tetrachloro-1,1',3,3'-tetraethyl-imidacarbocyanine iodide (JC-1) assay kit and 4,6-diamidino-2-phenylindole (DAPI) were from Beyotime Biotechnology (Shanghai, China). BODIPY-581/591C11 reagent, MitoTracker, and Singlet Oxygen Sensor Green (SOSG) were purchased from Thermo Fisher Scientific Co., Ltd. (Carlsbad, California, UK). Cell Counting Kit-8 (CCK-8) assays were obtained from Dojindo (Kumamoto, Japan).

2.2. Synthesis of IRP NPs

Briefly, 50 mg of PLGA-PEG_{2,000}, 2 mg of IR780, and 1 mg of RSL-3 were dissolved in 2 mL of dichloromethane (CH₂Cl₂). Briefly, 200 μ L of ultra-pure water was added to the above oil phase mixture using the probe sonicator (Sonics & Materials Inc., USA) at an intensity of 60W for 3 min. Subsequently, 5 mL of 4% PVA aqueous solution was added to the above solution for the second emulsification at an intensity of 45W for 3 min. About 10 mL of isopropanol solution (2%) was added and magnetically stirred for 3 h to remove CH₂Cl₂. Finally, the IRP NPs were purified by centrifugation (11,000 rpm, 6 min). The PLGA encapsulated IR780, and RSL-3 nanoparticles were named IRP NPS. The same operation process was also applicable to the synthesis of IP NPs (PLGA encapsulated IR780 nanoparticles), except that RSL-3 was not added.

2.3. Characterization of IRP NPs

The internal structure of IRP NPs was observed by transmission electron microscopic (TEM, FEI Tecnai G2 F20, USA). The size and zeta potential were determined using dynamic light scattering (DLS, Malvern Instruments Ltd., UK). The UV-vis

absorption spectra of PLGA, free IR780, IP NPs, and IRP NPs were obtained using a UV-vis spectrophotometer (US-2550, Shimadzu, Japan). A calibration curve was drawn using absorbance obtained at different concentrations of IR780. The encapsulation efficiency of IR780 was calculated using the standard curve. The encapsulation efficiency of RSL-3 was also measured by high-performance liquid chromatography (HPLC; ShmadzuLC-2-1-AHT; Japan). To obtain the release profiles of IR780 and RSL-3, we dispersed IRP NPs into phosphate buffered saline (PBS) and transferred the mixture to a dialysis membrane. Then, the membrane was put into a glass bottle containing PBS. After shaking at 37°C for 2 h, the solution was divided into two groups. One group was irradiated with LIFU, and the other served as a control. Obtained 1 mL of solution at predetermined time points (0, 1, 2, 4, 8, 12, 18, and 24 h), and then added 1 mL of PBS to the bottle. UV-vis spectrophotometer and HPLC, respectively, were used to measure the concentrations of IR780 and RSL-3. ROS(¹O₂) production was assessed in vitro using fluorescence spectroscopy (RF-5301PC, Shimadzu, Japan) of SOSG ($\lambda_{ex}/\lambda_{em}$ = 504 nm/525 nm).

2.4. Cellular uptake and distribution

The murine TNBC cell line 4T1 was obtained from Chongqing Key Laboratory of Ultrasound Molecular Imaging and cultured in RPMI-1640 medium containing 10% fetal bovine serum and 1% penicillin-streptomycin at 37°C and 5% CO₂. 4T1 cells were seeded into glass-bottom cell culture dishes (1 \times 10⁵ cells per dish) and incubated overnight. DiI-labeled IRP NPs (1 mL, 50 μ g/mL) were co-incubated with 4T1 cells for different time points (0.5, 1, 2 and, 4 h). Then, the dishes were rinsed with PBS three times. After fixation with 4% paraformaldehyde, 200 μ L of DAPI was added to each dish (8 min). Then, cellular uptake was observed by the Laser Confocal Scanning Microscopic (CLSM, Nikon A1, Japan). To quantify intracellular uptake, 4T1 cells were seeded in 6-well plates (1 \times 10⁵ cells per well) and incubated overnight to reach 80%–90% confluency. DiI-labeled IRP NPs (1 mL, 50 μ g/mL) were co-incubated with 4T1 cells for different durations (0.5, 1, 2, and 4 h). Cells were digested and collected, then measured intracellular red fluorescence by flow cytometry (BD facsvantage se, USA).

To ascertain the mitochondria-targeting ability of IRP NPs, 4T1 cells (1 \times 10⁵ cells per dish) were incubated in CLSM dishes overnight. After incubating cells with 50 μ g/mL of DiI-labeled IRP NPs for 4 h, cells were rinsed with PBS and dyed with MitoTracker for 30 min to label mitochondria. The mitochondrial localization of IRP NPs was confirmed using CLSM. Furthermore, the Pearson correlation coefficient was measured. To evaluate the co-localization of nanoparticles and lysosomes, MitoTracker was replaced with LysoTracker after the corresponding treatment of cells.

2.5. In vitro ROS production detection

ROS production in cells was detected using the green fluorescent probe DCFH-DA ($\lambda_{ex}/\lambda_{em}$ = 488 nm/530 nm). 4T1 cells were seeded in CLSM dishes (1 \times 10⁵ cells per dish) and randomly distributed into six groups: Control, US, IP NPs, IRP

NPs, IP NPs+US, and IRP NPs+US. The concentration of IR780 in each group was 4 µg/mL. After corresponding treatments, the cells were incubated with DCFH-DA (10 µM) in each dish and imaged with CLSM after three times of PBS washing. The collected cells were subjected to ROS quantification analysis by flow cytometry.

2.6. Mitochondrial membrane potential assay

4T1 cells were seeded in CLSM dishes (1×10^5 cells per dish) and incubated overnight. Next, dishes were randomly divided into the above six groups and treated accordingly. The concentration of IR780 in each group was 4 µg/mL. Dishes were stained with JC-1 following the manufacturer's protocol. Cells treated as aforementioned were collected for flow cytometry.

2.7. Cell viability study and apoptosis assay

The following six groups were performed after overnight incubation. Add CCK-8 reagent to the cell culture medium of each group, measure the absorbance at 450 nm, and calculate the cell viability of each group of treatments. Apoptosis was detected by flow cytometry after double staining with Calcein-AM/propidium iodide.

2.8. Western blot analysis

The treated proteins in each group were subjected to gel electrophoresis, transfer, and blocking. Incubated the protein with anti-Caspase-3, anti-HIF-1 α , and anti-GPX4 antibodies overnight at 4 °C. Horseradish peroxidase-conjugated rabbit IgG secondary antibody was incubated for 1 h at room temperature on a shaker. Visualized and analyzed the protein bands.

2.9. LPO Accumulation

4T1 cells were seeded in CLSM dishes (1×10^5 cells per dish) and incubated overnight. After six different treatments, BODIPY-581/591C11 (5 µM, 20 min) was added to each of the different dishes for LPO staining. The dishes were rinsed three times with PBS and LPO accumulation was observed by CLSM and flow cytometry analysis.

2.10. PAI of IRP NPs and in vivo biodistribution

For in vitro, PAI (excitation wavelength: 780 nm) was performed on a series of concentrations of IRP NPs at 31.25, 62.5, 125, 250, and 500 µg/mL, and a calibration curve was drawn between the PA values and the concentrations. For in vivo PAI, tumor-bearing mice were injected intravenously with IRP NPs in PBS (10 mg/mL, 200 µL). Intratumoral PAI images were acquired at 0, 1, 3, 6, 12, 24, and 48 h, respectively. The signal intensity within the tumor was analyzed to determine the optimal enrichment time for IRP NPs. The fluorescence characteristics of IR780 endow IRP NPs with fluorescence imaging performance ($\lambda_{\text{ex}}/\lambda_{\text{em}} = 745 \text{ nm}/820 \text{ nm}$),

which can further evaluate the biodistribution of IRP NPs. Fluorescence imaging was performed on mice at different times after tail vein injection of IRP NPs.

2.11. Antitumor therapy efficacy in vivo

A subcutaneous xenograft model was established by subcutaneous injection of 4T1 cells in BALB/c mice and 30 tumor-bearing mice were randomly divided into the following six groups: Control, US, IP NPs, IRP NPs, IP NPs+US, and IRP NPs+US. Twenty-four hours later, the different materials were injected through the tail vein of mice (10 mg/mL, 200 µL). We irradiated the tumor region of the mice with LIFU (on 2 min, off 2 min, two cycles) at 3 W/cm². Repeat the same operation on the third day. During the 14-day treatment period, mice's body weight and tumor volume were recorded every two days. After the treatment, tumors and major organs were collected for hematoxylin and eosin (H&E) and TdT-dependent dUTP-biotin nick end labeling (TUNEL) and HIF-1 α staining.

2.12. Biosafety of IRP NPs

Using healthy mice as an animal model for the biosafety of IRP NPs, we injected IRP NPs intravenously (10 mg/mL, 200 µL). Mice were sacrificed at specific time points (1, 7, and 14 days) after intravenous injection of IRP NPs, blood was collected for blood routine and biochemical tests, and major organs were collected for H&E staining.

2.13. Statistical analysis

All experiments were repeated at least three times, and the data are shown as mean \pm standard deviation. The Student's *t* tests determined statistical comparisons between groups (**p* < .05, ***p* < .01, ****p* < .001, *****p* < .0001).

3. Results and discussion

3.1. Design, synthesis, and characterization of IRP NPs

IRP NPs were synthesized through a typically double-emulsion approach (Deng et al., 2017), in which IR780 and RSL-3 were stably embedded in the PLGA shell. TEM characterization revealed that IRP NPs have a uniform spherical structure (Figure 1(a)). The average size of IRP NPs measured by a DLS system was 201.0 nm, consistent with the TEM results (Figure 1(b)). The zeta potential result exhibited an average potential of -5.49 mV (Figure 1(b)). The UV-vis spectrum of IR780 in different concentrations of dichloromethane showed a typical absorption peak near 780 nm. Both IRP NPs and IP NPs showed the characteristic absorption of free IR780, implying that the drug was successfully loaded (Figure 1(c)). The UV-vis spectrum absorption intensity of IR780 is concentration-dependent and has a good linear correlation shows a concentration (Figure 1(d,e)). The encapsulation rate of IR780 in IP NPs and IRP NPs was calculated to be 80.67% and 74.7%, respectively. The encapsulation rate of RSL-3 IRP NPs was 68.81%, obtained by HPLC. Compared with the

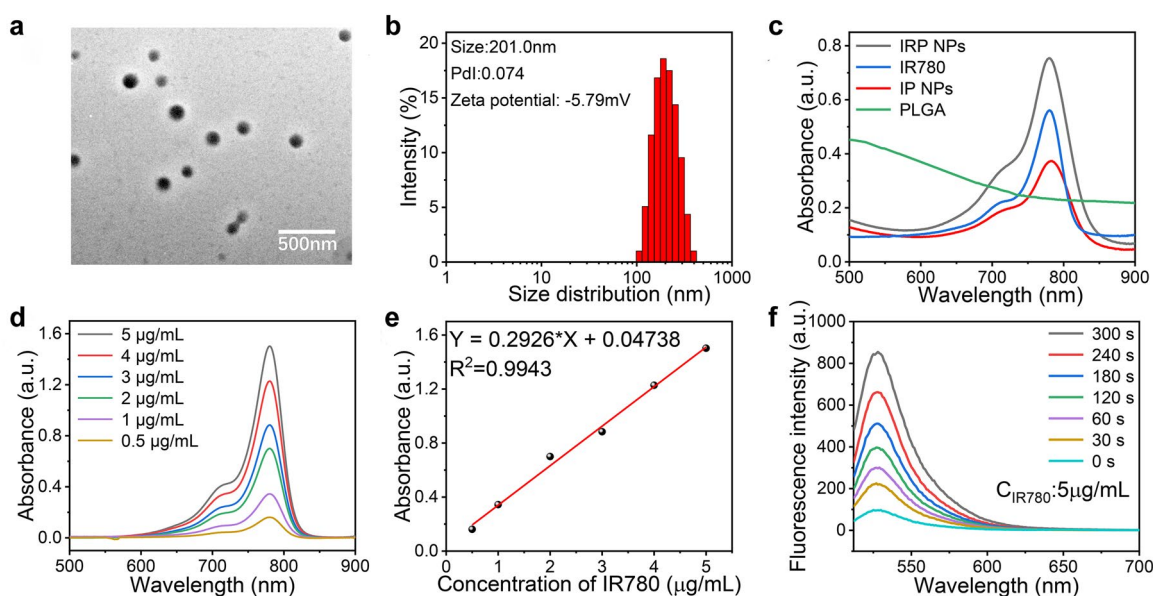


Figure 1. Characterizations of IRP NPs. (a) TEM of IRP NPs. (b) Size distribution, Pdl, and Zeta potential of IRP NPs. (c) Absorbance spectra of different NPs (PLGA, Free IR780, IP, IRP) as recorded by UV-vis spectra. (d) UV-vis absorbance spectra of free IR780 in different concentrations. (e) The standard curve of IR780 and UV-vis absorbance. (f) Time-dependent $^1\text{O}_2$ generation of IRP NPs irradiated by US.

irradiation group without LIFU, LIFU irradiation caused the rapid release of IR780 and RSL-3, which may be due to the rapid and enhanced release of drugs caused by the oscillation and cavitation effects caused by LIFU (Supplementary Figure S1 and S2). To study the efficiency of SDT, the generated ROS was measured by SOSG. IRP NPs have the ability to produce $^1\text{O}_2$ under US irradiation, and the fluorescence intensity increases with the irradiation time, which laid the foundation for the later SDT treatment (Figure 1(f)).

3.2. Cellular uptake and subcellular accumulation

The uptake of nanoparticles by tumor cells is the basis for subsequent therapy (Adjei et al., 2014). To assess the cellular uptake of IRP NPs by 4T1 cells, we labeled IRP NPs with red fluorescent dye Dil and incubated them with cells at different times. The CLSM and flow cytometric analysis showed that IRP NPs could be internalized by cells in a time-dependent manner (Figure 2(a,b)). That is to say, with the prolongation of incubation time, the uptake of IRP NPs in 4T1 cells gradually increased.

The subcellular localization of nanomaterials can significantly affect the therapeutic efficiency of tumors (Liew et al., 2021). Due to the inherent lipophilicity and overall positive charge of IR780, these compounds usually accumulate in mitochondria (Zhang et al., 2010). In order to study this result, after the Dil-labeled NPs were incubated with MitoTracker, the subcellular localization was studied by CLSM, and the intracellular luminescence patterns were compared. The red fluorescence of Dil-labeled NPs overlapped well with the green fluorescence of MitoTracker. The co-localization coefficient was 0.89, indicating that IRP NPs had mitochondrial targeting (Figure 2(c)). Comparatively, the poor overlap was observed in the case of LysoTracker (Supplementary Figure S3).

3.3. In vitro SDT and ferroptosis effects of IRP NPs

3.3.1. In vitro ROS production detection

Studies have shown that ROS production is tightly associated with SDT and ferroptosis. ROS triggers substantial modification of biomolecules at the cellular level, thus activating the apoptosis pathway (Su et al., 2019). The intracellular ROS generation capability of IRP NPs was detected by a ROS probe (DCFH-DA). According to Figure 3(a), cells treated with IRP NPs and IP NPs+US groups showed similarly strong green fluorescence and the most ROS in IRP NPs+US group. The results of flow cytometry showed that 4T1 cells treated with IRP NPs exhibited significant ROS compared to the control group (32.2%, Figure 3(b)). This also means RSL-3 could promote ROS production in 4T1 cells. The most vigorous green fluorescence intensity in the IRP NPs+US group (92.4%) was markedly higher than IP NPs (71.5%). The above results confirm that both RSL-3 and SDT can generate ROS, and the two have a significant synergistic effect.

3.3.2. Mitochondrial membrane potential assay

Selective subcellular accumulation of IRP NPs in the mitochondria of 4T1 cells has been previously validated. Then, the effects of IRP NPs mediated mitochondrial-targeted SDT, and ferroptosis on mitochondrial membrane potential were tested with the JC-1 probe. The cells in the IRP NPs combined with the US irradiation group experienced mitochondrial membrane potential decreased significantly and showed enhanced green and weak red fluorescence (Figure 4(a)). The quantitative results of JC-1 aggregates and JC-1 monomers were measured by flow cytometry. The degree of mitochondrial depolarization was calculated as the red to green fluorescence intensity ratio (Figure 4(b)). The results are consistent with CLSM. These results confirmed that IRP NPs combined with US irradiation reduced mitochondrial

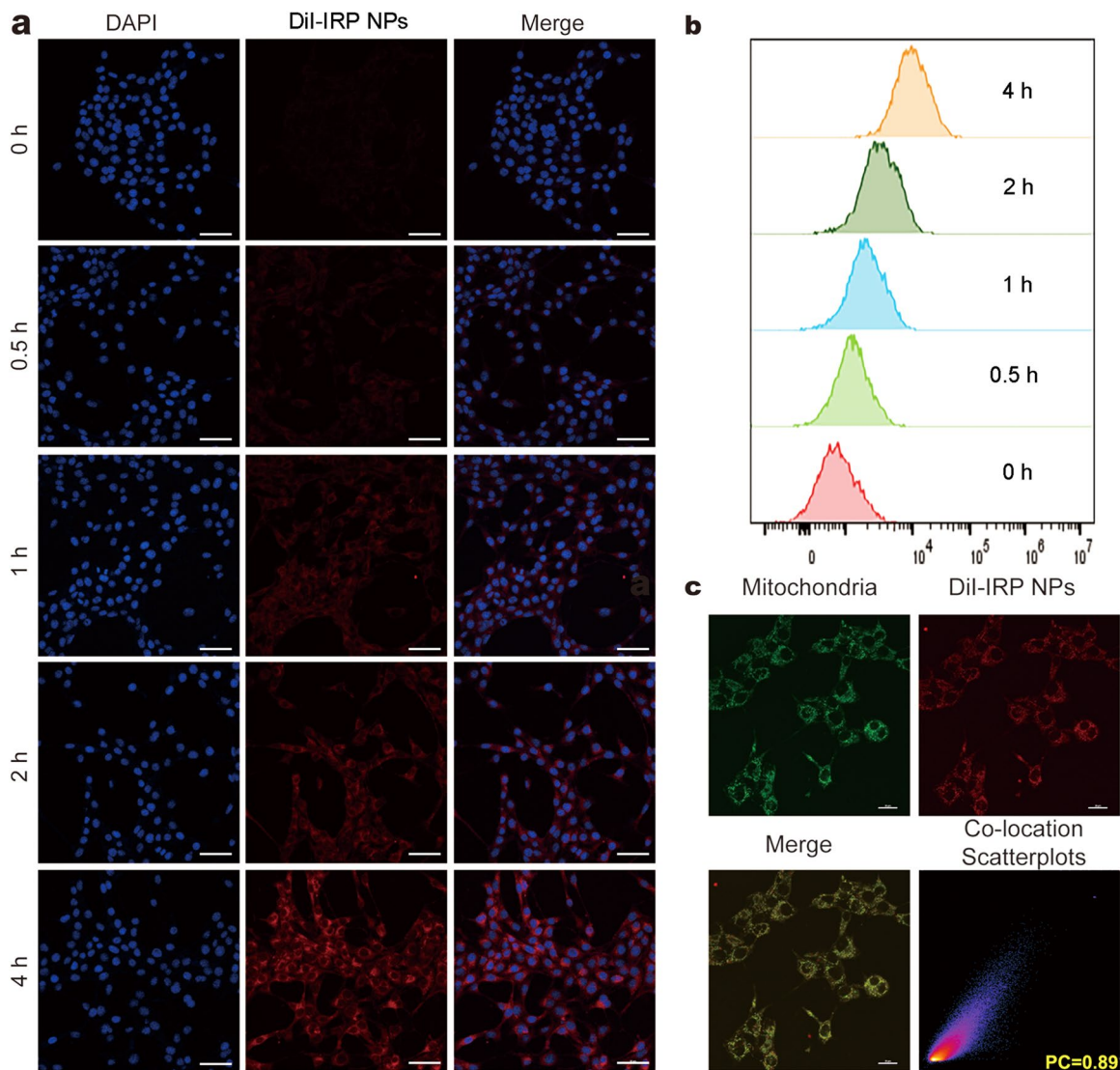


Figure 2. Cellular uptake behaviors and subcellular accumulation of IRP NPs. (a) Cellular uptake of IRP NPs observed using CLSM (scale bar: 50 μ m). (b) Cellular uptake of DiI-labeled IRP NPs by flow cytometry analysis. (c) Mitochondrial location of DiI-labeled IRP NPs as monitored by MitoTracker (scale bar: 20 μ m).

membrane potential and disrupted mitochondrial membrane integrity to synergize SDT against TNBC.

3.3.3. Cell viability study and apoptosis assay

After witnessing the enhanced SDT effect after using RSL-3, we then evaluated the cytotoxicity of IRP NPs on 4T1 cells in vitro by CCK-8 assay and apoptosis assay. The CCK-8 assay shown in Figure 5(a) shows that the IP NPs group and IRP NPs showed a slight decrease in cell viability. The cell viability of IRP NPs+US group decreased more significantly than that of IP NPs+US group. The results showed that synergistic therapy was more effective than monotherapy in cytotoxicity.

Next, Annexin V-FITC and PI staining assay was harnessed to detect further the apoptosis of 4T1 cells treated with different methods by flow cytometry (Figure 5(b)). IRP NPs+US group induces 54.2% of cell apoptosis, which distinctly exceeds the IP NPs+US group (33.6%). In conclusion, the results consistently show that IRP NPs have the most effective cytotoxicity, and RSL-3 can enhance the therapeutic effect of SDT.

3.3.4. Western blot analysis

Furthermore, as shown in Figure 5(c,d), we detected the expression of the caspase-3 protein (a typical apoptotic signal) by western blot (WB). We found that the expression of Caspase-3 in SDT combined with the ferroptosis group loaded with RSL-3 was significantly higher than in the SDT group.

Next, we explored the possible mechanism of RSL-3 synergizing SDT. GSH and GPX4 are the central antioxidant systems in vivo, and GPX4 is the glutathione-dependent lipid repair enzyme. When SDT mediates ROS production, RSL-3 can inactivate GPX4 and increase intracellular LPO levels, which is an essential indicator of ferroptosis. Next, WB was used to verify the expression of GPX4 (Figure 5(e,f)). When RSL-3 was present, the expression of GPX4 decreased, and that of the IRP NPs+US group decreased significantly.

In addition, SDT-induced ROS production exacerbates tumor hypoxia, which increases HIF-1 α levels and induces increased vascular endothelial growth factor expression, promoting tumor growth and metastasis (Kim et al., 2016; Goyette et al., 2021). Therefore, we also used WB to study the effect of RSL-3 on HIF-1 α Expression (Figure 5(g,h)). The results showed that SDT

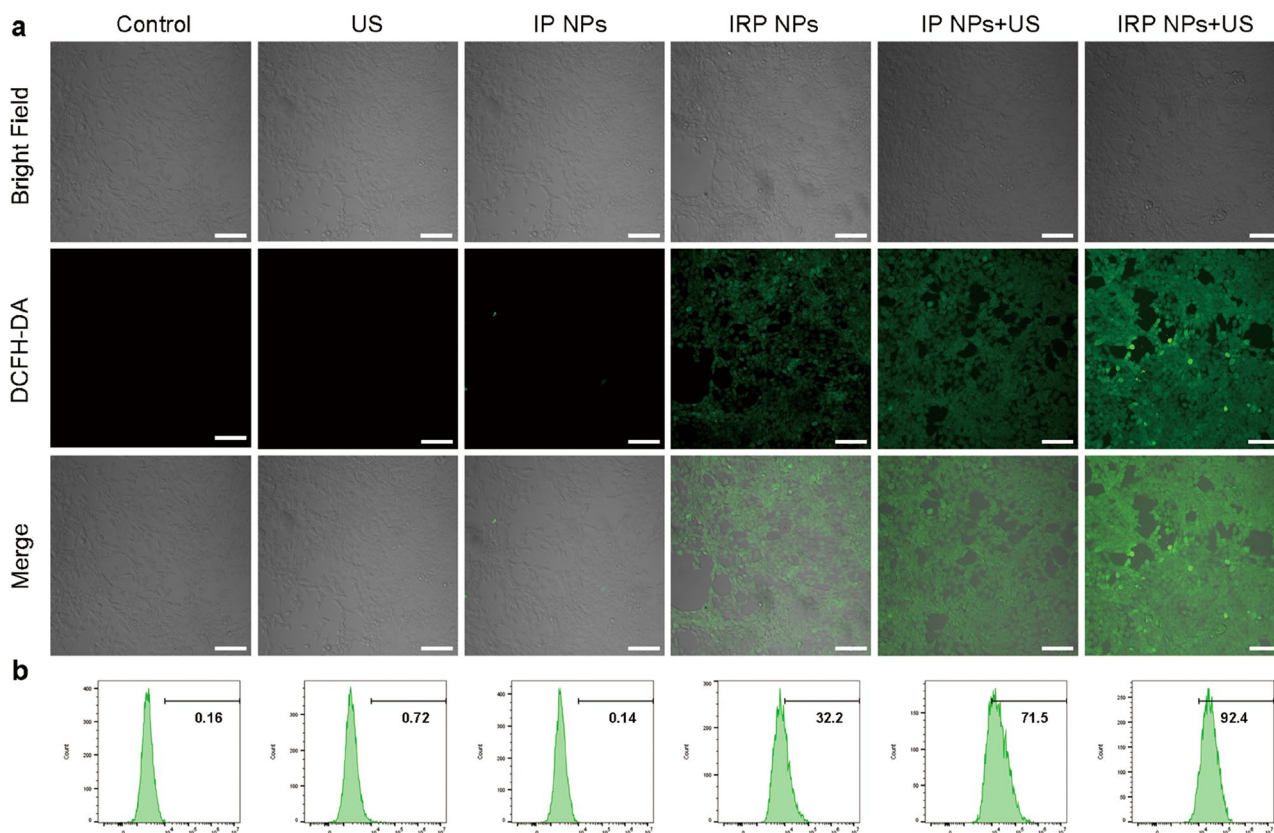


Figure 3. Intracellular ROS generation of IRP NPs. (a) The intracellular ROS levels were determined by DCFH-DA probe reagent and imaged by CLSM images of 4T1 cells (scale bar: 100 μ m). (b) The intracellular ROS levels were stained with DCFH-DA probe reagent and detected by flow cytometry.

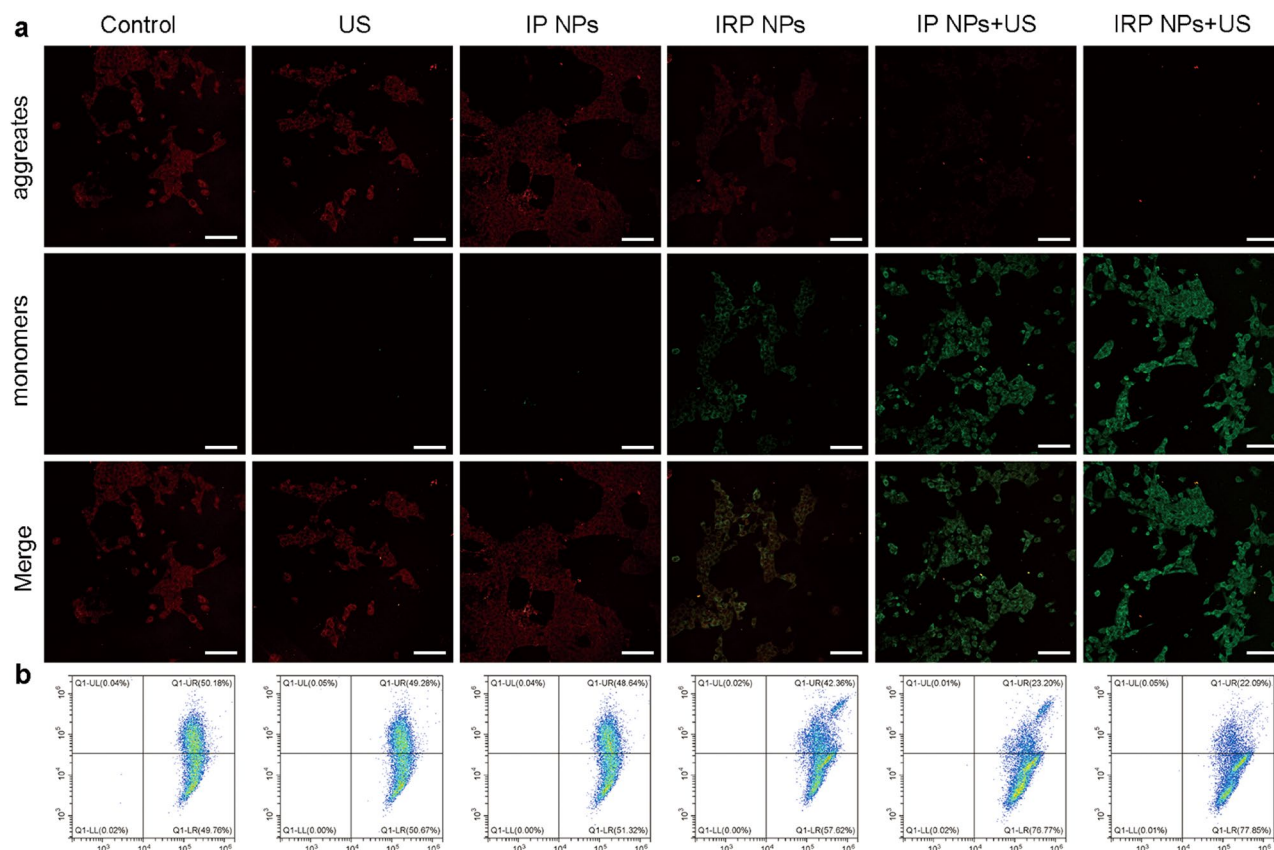


Figure 4. Mitochondria membrane potential. (a) Mitochondria membrane potential changes of 4T1 cells after corresponding treatments observed using CLSM (scale bar: 100 μ m). (b) JC-1 assay as a measure of mitochondrial depolarization by flow cytometry.

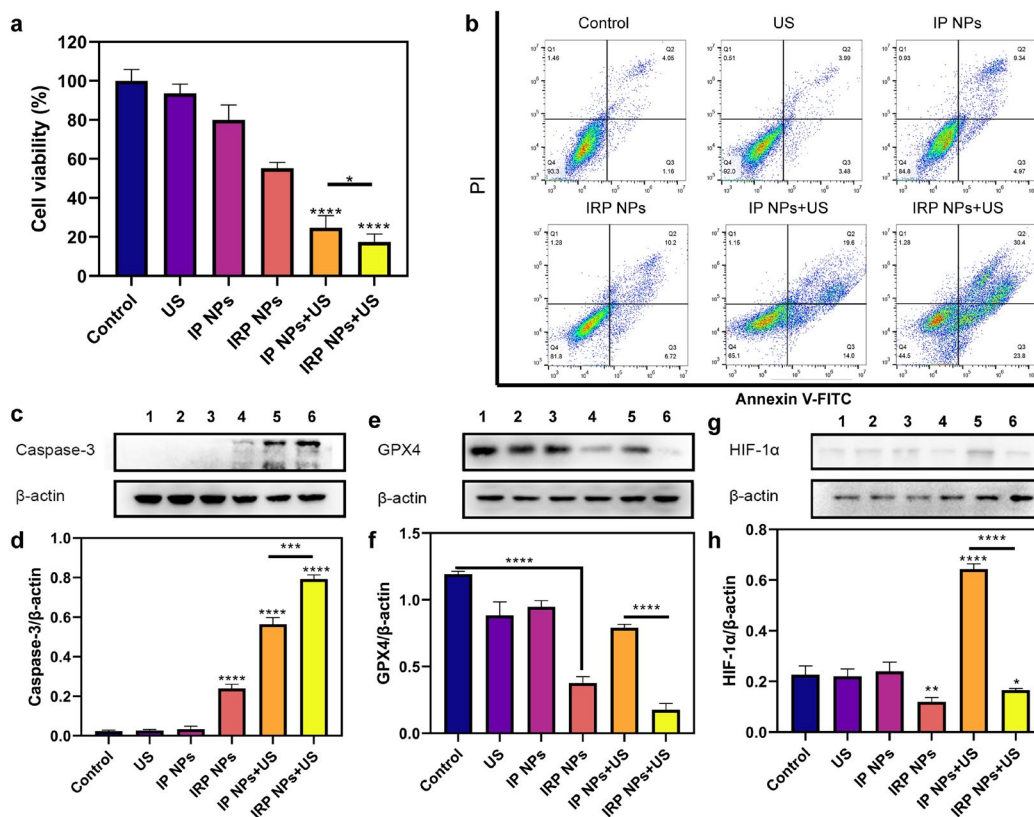


Figure 5. In vitro SDT and ferroptosis effects of IRP NPs. (a) Cell viability of 4T1 cells after different treatments was tested via CCK-8 assay. (b) The apoptosis of 4T1 cells with different treatments was detected by flow cytometry. (c and d) Western blot analysis of Caspase-3 expression in 4T1 cells after the corresponding treatments and quantitative analysis of the Caspase-3 expression. (e and f) Western blot analysis of GPX4 expression in 4T1 cells after the different treatments and quantitative analysis of the GPX4 expression. (g and h) Western blot analysis of HIF-1 α expression in 4T1 cells after the different treatments and quantitative analysis of the HIF-1 α expression.

increased the expression of HIF-1 α , whereas RSL-3 inhibited the upregulation of HIF-1 α expression. This suggests that RSL-3 can alleviate tumor hypoxia and enhance treatment.

3.3.5. LPO accumulation

A fundamentally different marker of ferroptosis is the presence of LPO, whose accumulation contributes to the occurrence of ferroptosis (Ursini & Maiorino, 2020). To study whether LPO was produced in cancer cells during treatment, 4T1 cells were incubated with fluorescent LPO-specific dye BODIPY-581/591C11 reagent after various treatments. The results showed that the polyunsaturated butadiene in BODIPY-581/591C11 reagent was partially oxidized by lipid reactive oxygen species (lipid ROS), and the maximum excitation wavelength shifted from 590 nm to 510 nm. The probe still maintained lipophilicity. It can show the level of intracellular lipid ROS. CLSM showed red weakening, and green enhancement (Figure 6(a)). IRP NPs+US group showed the weakest red and the strongest red light, indicating the most LPO accumulation. The amount of LPO was further confirmed by flow cytometry (Figure 6(b)). These results showed that the levels of apoptosis and ferroptosis were the highest in the IRP NPs+US group, which synergistically treated tumors.

3.4. PAI of IRP NPs

PA imaging has practical significance in monitoring the accumulation of IRP NPs in tumor areas and guiding tumor

treatment in real time. IR780 can be used as a PA contrast agent. We used VEVO LAZR photoacoustic imaging system to perform PA imaging on IRP NPs and 780 nm as excitation wavelength for PAI. As shown in Figure 5(a), the signal intensity of IRP NPs has a clear concentration dependence, which increases from 0.171 to 0.611 with the concentration of IRP NPs (31.25, 62.5, 125, 250, and 500 $\mu\text{g}/\text{mL}$). We then tested the imaging capabilities of IRP NPs in a xenograft model. IRP NPs were injected into the caudal vein to verify whether they could accumulate in the tumor area. The PA signal in the tumor area was observed after 1 h and peaked after 24 h of injection (Figure 7(b,c)). We can verify by PAI that IRP NPs can be enriched within the tumor region. PAI can help evaluate the time of ultrasound intervention and guide the visual treatment process. In vivo fluorescence imaging showed that after injection of IRP NPs, IRP NPs first aggregated in the liver, transferred to the spleen and tumor over time, and finally enriched in the tumor and metabolically attenuated (Supplementary Figure S4).

3.5. In vivo antitumor capacity

IRP NPs show the potential to overcome the obstacles of tumor treatment. Next, we will study the in vivo anticancer activity. Next, thirty 4T1 tumor-bearing mice were randomly divided into six groups (control, US, IP NPs, IRP NPs, IP NPs+US, and IRP NPs). The tumor volume of mice and body weight were monitored every two days to plot the growth curve. The control group and US group increased rapidly

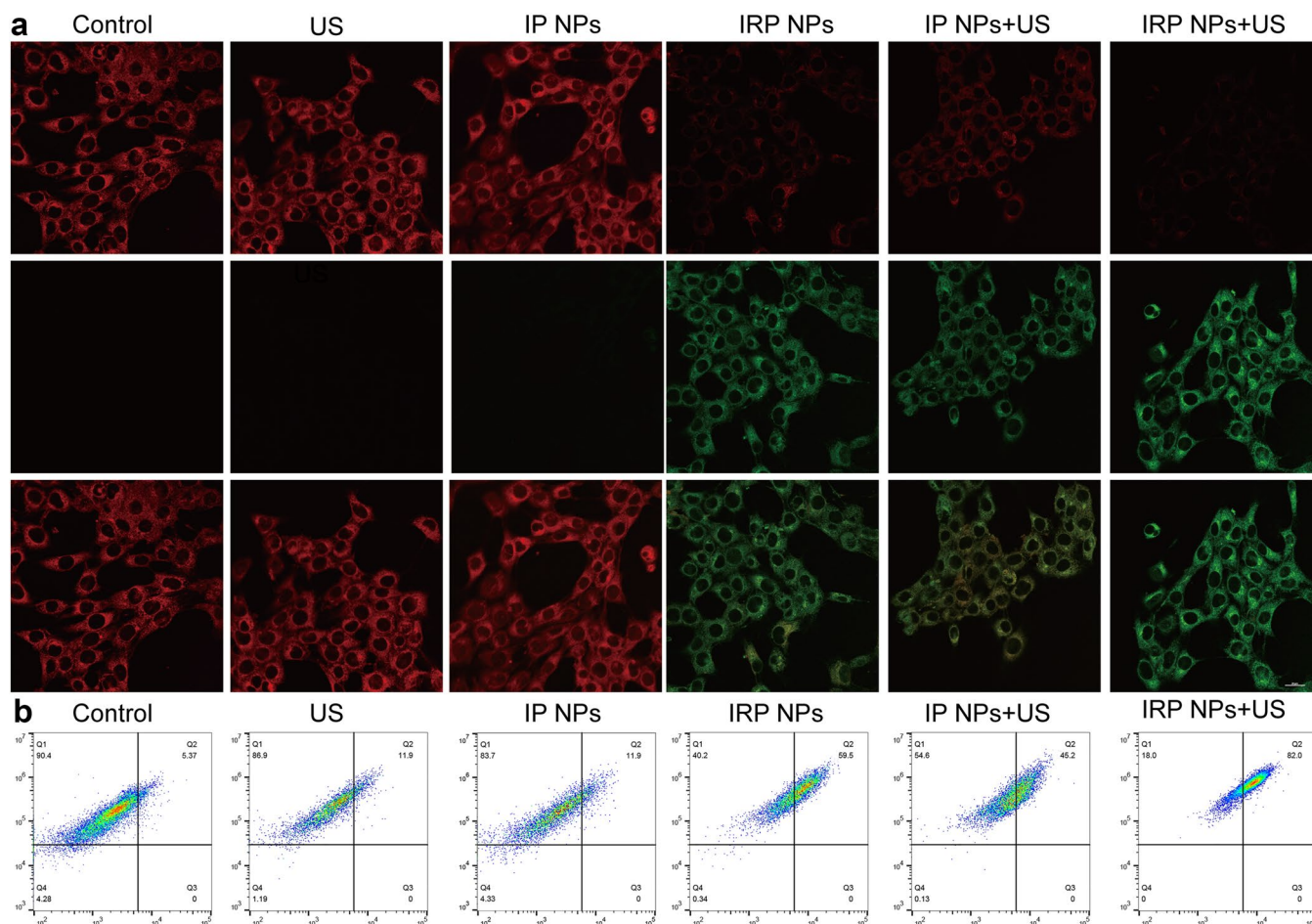


Figure 6. LPO accumulation. (a) LPO accumulation of cells after different treatments observed by CLSM (scale bar: 20µm). (b) Flow-cytometry-based LPO accumulation assay.

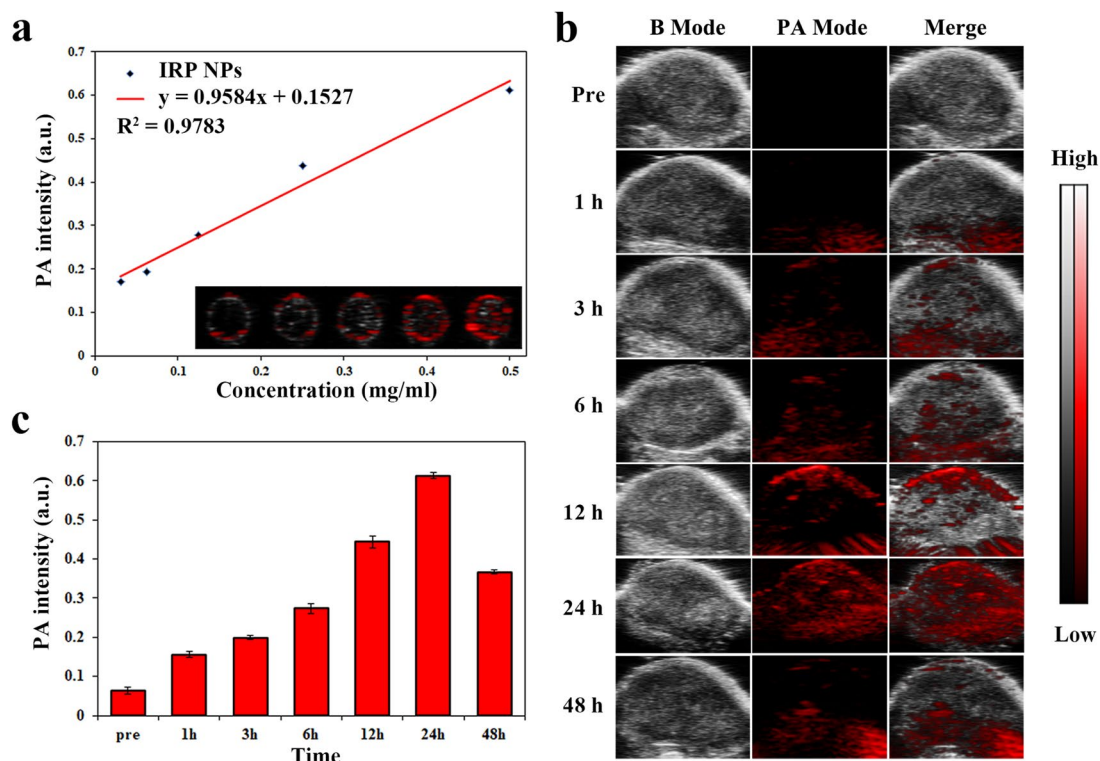


Figure 7. PAI of IRP NPs. (a) The standard curve of PA signal intensity and the concentration of IRP NPs (31.25, 62.5, 125, 250, and 500µg/mL). (b) PAI of tumors injection of IRP NPs at different time points. (c) The PA signal intensity of IRP NPs in tumor region at different time points.

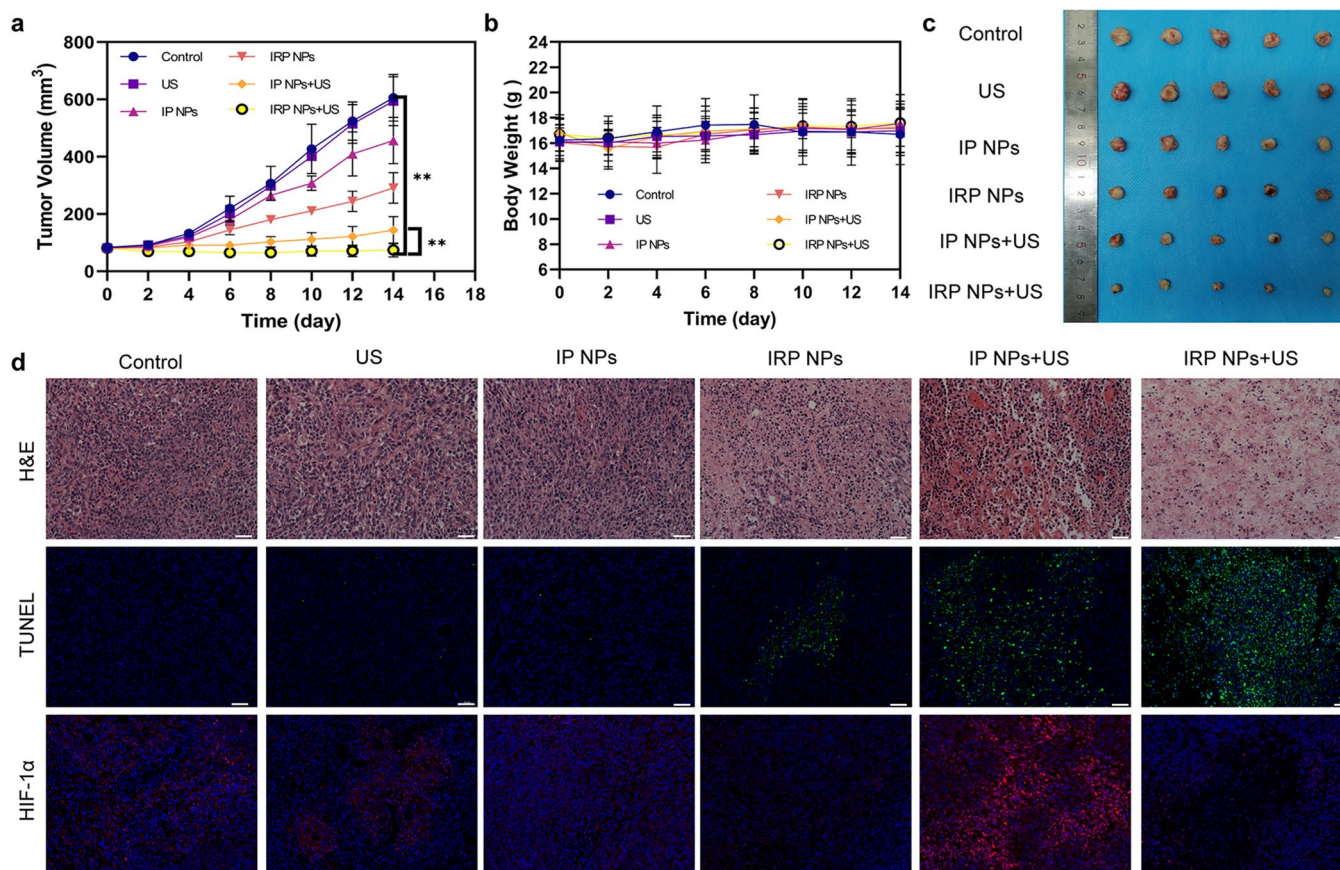


Figure 8. In vivo antitumor effect of IRP NPs. (a) Time-dependent tumor volume curves after different treatments ($n=5$). (b) Time-dependent body weights curves after different treatments ($n=5$). (c) Photographs of tumors in each group after treatments. (d) H&E, TUNEL, and HIF-1 α staining of tumor regions after different treatments (scale bar: 50 μm).

during the whole treatment period, illustrating that the use of PBS and US alone did not affect limiting tumor growth (Figure 8(a)). The tumor growth of the IP NPs+US group was significantly inhibited, which was related to a large amount of ROS produced during SDT. The tumor growth trend of the IRP NPs+US group was further inhibited. This fantastic therapeutic effect can be attributed to the synergistic effect of RSL-3-mediated ferroptosis and SDT-mediated apoptosis. No significant weight loss or difference was found during treatment (Figure 8(b)). After 14 days of treatment, the mice tumor was removed, and digital photos were taken (Figure 8(c)).

Next, we stained the treated tumors in each group for H&E and TUNEL staining (Figure 8(d)). It was found that severe cell damage occurred in the IRP NPs+US group, which proved the effectiveness of synergistic therapy. After confirming the efficacy, we also measured HIF-1 α in tumors (Figure 8(d)). To study the role of RSL-3 in enhancing SDT. It can be seen from the immunofluorescence staining image that SDT can induce the upregulation of HIF-1 α (Wang et al., 2018; Zhang et al., 2021a). This may further increase the hypoxia of the tumor. Therefore, RSL-3 can enhance the therapeutic effect of SDT by inhibiting HIF-1 α . The above results confirmed the therapeutic advantage of SDT combined with ferroptosis. IRP NPs+US group can effectively induce ferroptosis and increase the susceptibility of 4T1 cells to SDT and induce more cells to undergo apoptosis.

Moreover, H&E staining was performed on major organs, including the mice's heart, liver, spleen, lung, and kidney after treatment (Figure 9). Compared to the control group, no significant histopathological necrosis, hydropic degeneration, and inflammation lesions could be observed after different treatments, demonstrating the high biocompatibility of IRP NPs.

3.6. Biosafety of IRP NPs

Finally, we studied the potential toxicity of IRP NPs in healthy mice. After tail vein injection, the main organs and blood samples were collected at a predetermined time for analysis. The main parameters of routine blood tests and biochemistry remained stable without noticeable changes (Figure 10(a)). In addition, no inflammation or tissue damage was observed in the main organs of the mice (Figure 10(b)). All these data prove that IRP NPs have good biocompatibility.

4. Conclusions

In conclusion, a novel mitochondria-targeting nanosystem ('Mito-Bomb') for ferroptosis-boosted SDT was presented. The nanosystem was selectively localized in the mitochondria of TNBC cells, and ultrasound irradiation resulted in the loss of mitochondrial membrane potential and mitochondrial damage, thereby triggering cell death through a combination of

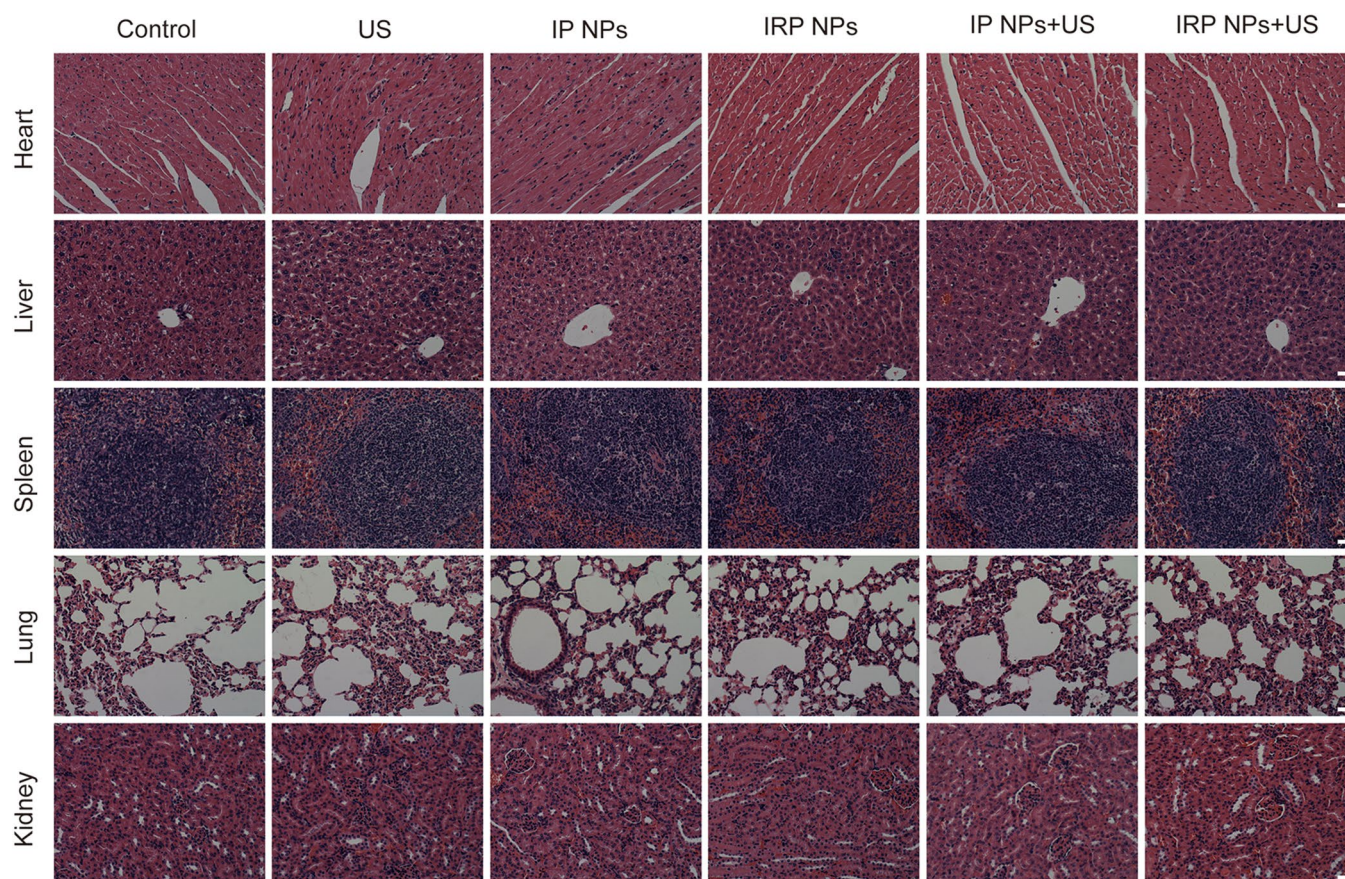


Figure 9. H&E staining of heart, liver, spleen, lung, and kidney after different treatments (scale bar: 50 μ m).

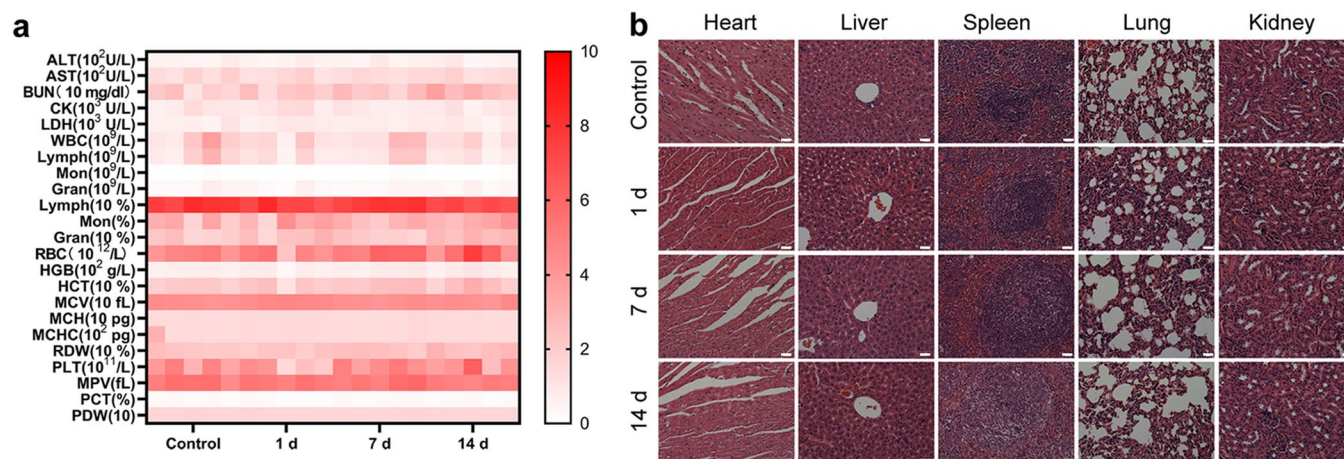


Figure 10. Biosafety of IRP NPs. (a) Biochemical assay and hematology analysis of mice intravenously injected with IRP NPs. The blood samples were collected at pre-determined time points (0, 1, 7, and 14 d) post-injection. (b) H&E staining of tissue sections from major organs after treatments (scale bar: 50 μ m).

ferroptosis and apoptotic pathways. In addition, the excellent biosafety of IRP NPs makes them more valuable for clinical translation.

Author contributions

Jianxin Wang: Methodology, Investigation, Software, Writing – original draft; Zhiyu Zhao: Software, Investigation, Visualization; Yan Liu: Software, Methodology; Xinyu Cao: Methodology, Supervision; Fuxin Li: Visualization; Haitao Ran:

Resources, Supervision Yang Cao: Conceptualization, Resources, Writing – review & editing; Changjun Wu: Conceptualization, Project administration, Supervision, Resources, Writing – review & editing,

Disclosure statement

The authors declare that they have no known competing financial interests or personal relationships that could have appeared to influence the work reported in this paper.

Funding

This work was supported by the National Natural Science Foundation of China (No. 82071926 and 81630047), the University Innovation Team Plans of Chongqing under grants (No. CXTDG201602007.)

References

- Adjei IM, Sharma B, Labhassetwar V. (2014). Nanoparticles: cellular uptake and cytotoxicity. *Adv Exp Med Biol* 811:73–91.
- Deng L, Cai X, Sheng D, et al. (2017). A laser-activated biocompatible theranostic nanoagent for targeted multimodal imaging and photothermal therapy. *Theranostics* 7:4410–23.
- Dixon SJ, Lemberg KM, Lamprecht MR, et al. (2012). Ferroptosis: an iron-dependent form of nonapoptotic cell death. *Cell* 149:1060–72.
- Eaton JK, Furst L, Ruberto RA, et al. (2020). Selective covalent targeting of GPX4 using masked nitrile-oxide electrophiles. *Nat Chem Biol* 16:497–506.
- Glickman RD. (2021). Photoacoustic imaging and sensing: a new way to see the eye. *J Ocul Pharmacol Ther* 37:162–71.
- Goyette MA, Elkholi IE, Apcher C, et al. (2021). Targeting Axl favors an anti-tumorigenic microenvironment that enhances immunotherapy responses by decreasing Hif-1 α levels. *Proc Natl Acad Sci USA* 118:e2023868118.
- Guo X, Yang N, Ji W, et al. (2021). Mito-Bomb: targeting mitochondria for cancer therapy. *Adv Mater* 33:e2007778.
- Han X, Song Z, Zhou Y, et al. (2021). Mitochondria-targeted high-load sound-sensitive micelles for sonodynamic therapy to treat triple-negative breast cancer and inhibit metastasis. *Mater Sci Eng C Mater Biol Appl* 124:112054.
- Hirschhorn T, Stockwell BR. (2019). The development of the concept of ferroptosis. *Free Radic Biol Med* 133:130–43.
- Jiang F, Yang C, Ding B, et al. (2022). Tumor microenvironment-responsive MnSiO₃-Pt@BSA-Ce₆ nanoplatfor for synergistic catalysis-enhanced sonodynamic and chemodynamic cancer therapy. *Chin Chem Lett* 33:2959–64.
- Kim Y, Nam HJ, Lee J, et al. (2016). Methylation-dependent regulation of HIF-1 α stability restricts retinal and tumour angiogenesis. *Nat Commun* 7:10347.
- Lafond M, Yoshizawa S, Umemura SI. (2019). Sonodynamic therapy: advances and challenges in clinical translation. *J Ultrasound Med* 38:567–80.
- Li J, Cao F, Yin HL, et al. (2020). Ferroptosis: past, present and future. *Cell Death Dis* 11:88.
- Li X, Luo R, Liang X, et al. (2022). Recent advances in enhancing reactive oxygen species based chemodynamic therapy. *Chin Chem Lett* 33:2213–30.
- Liew SS, Qin X, Zhou J, et al. (2021). Smart design of nanomaterials for mitochondria-targeted nanotherapeutics. *Angew Chem Int Ed Engl* 60:2232–56.
- Luo L, Wang H, Tian W, et al. (2021). Targeting ferroptosis-based cancer therapy using nanomaterials: strategies and applications. *Theranostics* 11:9937–52.
- Pathania D, Millard M, Neamati N. (2009). Opportunities in discovery and delivery of anticancer drugs targeting mitochondria and cancer cell metabolism. *Adv Drug Deliv Rev* 61:1250–75.
- Qu F, Wang P, Zhang K, et al. (2020). Manipulation of mitophagy by "All-in-One" nanosensitizer augments sonodynamic glioma therapy. *Autophagy* 16:1413–35.
- Shintoku R, Takigawa Y, Yamada K, et al. (2017). Lipoxygenase-mediated generation of lipid peroxides enhances ferroptosis induced by erastin and RSL3. *Cancer Sci* 108:2187–94.
- Son S, Kim JH, Wang X, et al. (2020). Multifunctional sonosensitizers in sonodynamic cancer therapy. *Chem Soc Rev* 49:3244–61.
- Steinberg I, Huland DM, Vermesh O, et al. (2019). Photoacoustic clinical imaging. *Photoacoustics* 14:77–98.
- Stockwell BR, Friedmann Angeli JP, Bayir H, et al. (2017). Ferroptosis: a regulated cell death nexus linking metabolism, redox biology, and disease. *Cell* 171:273–85.
- Su LJ, Zhang JH, Gomez H, et al. (2019). Reactive oxygen species-induced lipid peroxidation in apoptosis, autophagy, and ferroptosis. *Oxid Med Cell Longev* 2019:5080843.
- Sun LL, Linghu DL, Hung MC. (2021). Ferroptosis: a promising target for cancer immunotherapy. *Am J Cancer Res* 11:5856–63.
- Tang D, Chen X, Kang R, et al. (2021). Ferroptosis: molecular mechanisms and health implications. *Cell Res* 31:107–25.
- Ursini F, Maiorino M. (2020). Lipid peroxidation and ferroptosis: the role of GSH and GPX4. *Free Radic Biol Med* 152:175–85.
- Wang L, Niu M, Zheng C, et al. (2018). A core-shell nanoplatfor for synergistic enhanced sonodynamic therapy of hypoxic tumor via cascaded strategy. *Adv Healthc Mater* 7:e1800819.
- Wang YW, Fu YY, Peng Q, et al. (2013). Dye-enhanced graphene oxide for photothermal therapy and photoacoustic imaging. *J Mater Chem B* 1:5762–7.
- Wei Y, Lv H, Shaikh AB, et al. (2020). Directly targeting glutathione peroxidase 4 may be more effective than disrupting glutathione on ferroptosis-based cancer therapy. *Biochim Biophys Acta Gen Subj* 1864:129539.
- Xu C, Sun S, Johnson T, et al. (2021). The glutathione peroxidase Gpx4 prevents lipid peroxidation and ferroptosis to sustain Treg cell activation and suppression of antitumor immunity. *Cell Rep* 35:109235.
- Yang WS, SriRamaratnam R, Welsch ME, et al. (2014). Regulation of ferroptotic cancer cell death by GPX4. *Cell* 156:317–31.
- Yao X, Xie R, Cao Y, et al. (2021). Simvastatin induced ferroptosis for triple-negative breast cancer therapy. *J Nanobiotechnol* 19:311.
- Zhang C, Liu T, Su Y, et al. (2010). A near-infrared fluorescent heptamethine indocyanine dye with preferential tumor accumulation for in vivo imaging. *Biomaterials* 31:6612–7.
- Zhang L, Wang D, Yang K, et al. (2018). Mitochondria-targeted artificial "Nano-RBCs" for amplified synergistic cancer phototherapy by a single NIR irradiation. *Adv Sci (Weinh)* 5:1800049.
- Zhang P, Zhang L, Wang J, et al. (2021a). An intelligent hypoxia-relieving chitosan-based nanoplatfor for enhanced targeted chemo-sonodynamic combination therapy on lung cancer. *Carbohydr Polym* 274:118655.
- Zhang Y, Zhang X, Yang H, et al. (2021b). Advanced biotechnology-assisted precise sonodynamic therapy. *Chem Soc Rev* 50:11227–48.
- Zong WX, Rabinowitz JD, White E. (2016). Mitochondria and Cancer. *Mol Cell* 61:667–76.